Customizing acoustic dirac cones and topological insulators in square lattices by topology optimization

Hao-Wen Dong [a,b], Sheng-Dong Zhao [c,d], Rui Zhu [e], Yue-Sheng Wang [f,*],
Li Cheng [a,*], Chuanzeng Zhang [g]

[a] *Department of Mechanical Engineering, The Hong Kong Polytechnic University, Hong Kong, China*
[b] *Department of Applied Mechanics, University of Science and Technology Beijing, Beijing 100083, China*
[c] *School of Mathematics and Statistics, Qingdao University, Qingdao 266071, China*
[d] *Institute of Mechanics for Multifunctional Materials and Structures, Qingdao University, Qingdao 266071, China*
[e] *School of Aerospace Engineering, Beijing Institute of Technology, Beijing 100081, China*
[f] *Department of Mechanics, School of Mechanical Engineering, Tianjin University, Tianjin 300350, China*
[g] *Department of Civil Engineering, University of Siegen, D-57068 Siegen, Germany*

ABSTRACT

Dirac point, the cornerstone of topological insulators, has been attracting ever-increasing attention due to its extraordinary properties. In this paper, a bottom-up topology optimization approach is established to systematically design the acoustic Dirac cones with customized double, triple and quadruple degeneracies at different wavelength scales. Using the proposed methodology, novel square-symmetric, chiral and orthogonal-symmetric sonic crystals (SCs) are constructed in a square lattice with tailored Dirac cones. The proposed design approach offers a unified framework to tailor SCs with exotic functionalities which are being widely researched in acoustic metamaterial community. As illustrative examples, zero-index acoustic cloaking and Talbot effect near the Dirac points of the optimized SCs are demonstrated numerically. Moreover, a novel acoustic pseudo-spin topological insulator is obtained, which entails a robust zigzag wave propagation and broadband, unidirectional, and topologically protected transport with a record-breaking relative bandwidth of 30.51%. The proposed design methodology shows promise and opens new horizons for customizing topological acoustics and conceiving high-efficiency wave devices.

© 2020 Elsevier Ltd. All rights reserved.

1. Introduction

Topological insulators have demonstrated extraordinary potential for optical [1,2], acoustic [3-15] and elastic [15-18] wave manipulations. Acoustic topological insulators [3-15] play a vital role in sound isolation, acoustic switch, acoustic split and integrated acoustic communications. For a system protected by the time-reversal symmetry, designing particular spatial symmetry [6] can form the electron-like pseudo time-reversal symmetry and pseudo-spin states, resulting in similar quantum spin-Hall effect. Besides, the quantum valley Hall effect [7] introduces the non-zero Berry curvature to form two chiral valley pseudo-spin states as well. The implementation, whether for TIs [1-18] or Weyl topological nodes [13], can be

---

* Corresponding author.
  E-mail addresses: yswang@tju.edu.cn (Y.-S. Wang), li.cheng@polyu.edu.hk (L. Cheng).

achieved through a proper design of Dirac cones [9,10,12-15]. Until now, conventional approaches consist in exploiting the lattice symmetry to generate the Dirac/Weyl point at the high-symmetry wave-vector point/line.

In the pursuit of customized topological acoustics, existing design strategies of Dirac cones and acoustic topological insulators suffer from some bottle-necking limitations, calling for effective solutions mainly in the following respects. Firstly, most published works use triangle or honeycomb lattices [14,15,19-22] in which the deterministic degeneracy can be easily modulated. Although square lattices [9,17] might provide a broader design space and might be more conducive to the design of high-order topological states [8,9], the issue has not been fully explored. Secondly, the structural configurations are restricted to the predetermined regular triangular, circular and elliptical scatters, thus limiting the design space and hindering the discovery of novel high-performance topology. Thirdly, most reported acoustic topological insulators only offer narrow-band topological states.

The aforementioned problems are largely due to the lack of a systematic design approach and associated simulation/optimization tools. An inverse approach which embraces a bottom-up philosophy should be the ideal option to meet the design target. Among possible choices is the topology optimization, which has successfully led to a series of novel wave properties [23-25]. One straightforward approach for the inverse design of topological insulators is directly maximizing the field intensity of an entire large device model [26,27] by introducing a given initial guess for the target spin-hall effect and robust transmission. Another strategy is a three-step design approach, i.e., firstly obtaining a single Dirac cone at the K point; then applying the specific zone folding to map the Dirac cone onto a double Dirac cone at the Γ point while expanding the unitcell size; and finally generating the non-trivial and trivial unitcells by breaking translational symmetry [38]. In addition, one can firstly optimize the band structure of a given structure with a single Dirac cone to realize the band inversion; and then optimize the supercells to maximize the operating bandwidth of the topological edge states [39]. Despite the recent attempts on topology optimization of topological optics [26], acoustics [27] and elasticity [38,39], systematic inverse design and customization of acoustic Dirac cones with tailored degeneracies and TIs based on predetermined pseudo-spin mechanism are still lacking. This motivated the present work.

In this paper, a bottom-up topology optimization approach is established for the structural design of topological acoustics. More specifically, we systematically perform the inverse design of sonic crystals (SCs) in square lattices to customize Dirac cones with different structural symmetries, degeneracies, and even eigenstate forms on demand. Common beneficial topological features of the optimized novel SCs at both short- and long-wavelength scales are revealed. Subsequently, it is demonstrated that the optimized short- and long-wavelength SCs with three-order Dirac cones can respectively give rise to the near-zero-index acoustic cloaking and Talbot effect near the Dirac point. Taking an optimized SC with customized double Dirac cones as the initial configuration, further topology optimization of SCs is conducted to generate two unitcells, which support topologically non-trivial and trivial bandgaps within two different given frequency ranges, thus constructing broadband pseudo-spin topological insulators in square lattices.

Apart from the proposal of a general design approach, this work also contributes to the existing knowledge in revealing new physical insights and obtaining multi-functional SCs with unprecedented performance. The claimed novelty is mainly twofold: 1) Novel square-latticed SCs with customized Dirac cones are obtained, whose beneficial topological features are demonstrated and the underlying mechanisms of Mie-resonance and LC-resonance (inductor-capacitor circuit) induced Bragg-scattering and subwavelength degeneracy are revealed; 2) Novel acoustic topological insulators, which exhibit unprecedented broadband feature, are obtained with required pseudo-spin mechanism. The proposed bottom-up inverse design methodology, as well as the optimized SCs with the customized Dirac cones and topological insulators, show great promise for realizing high-performance topological acoustic devices.

2. Topology optimization of customized acoustic dirac cones

Topological optics, acoustics and mechanics call for an elaborate design of crystal unitcells to achieve the ideal Dirac cone dispersions. Customizing the Dirac cones to achieve specific properties is a vital step to empower the SC unitcells with the required eigenstates. Here, we perform topology optimization to customize Dirac cones by exploiting the concept of local density of states (LDOS) [28], analogous to the power radiated by a polarized point source. The calculation of the LDOSs for different excitation sources is conducted by applying suitable even or odd boundaries [28] on the unitcell for the resulting modes. More specifically, a monopolar (M) mode has four even symmetries along the two principle directions; a dipolar (D) mode usually has two even symmetries along one principle direction and two odd symmetries in the other direction; a quadrupolar (Q) mode has four odd symmetries along the two principle directions. Note the principle directions can be manually selected as the axes with special angles rather than the x- and y- directions. With the above conditions, a given point source introduced in the unitcell induces a resonance mode when the LDOS is maximized. Consider the wave propagation in a solid/air system, in which the solid material is approximated as a fluid with very high stiffness and specific mass. For target resonance modes at a frequency f_0, the genetic algorithm (GA) [26–30] is used to maximize the responses under the specific point sources, forming the following optimization formulation of SCs:

$$Find : \rho_i = 0 \ or \ 1 \ (i = 1, 2, \ldots N \times N), \tag{1}$$

$$Maximize : L_{\min}(\Sigma, f_0) = \min_{i=1,2\cdots N_S} \left\{ -\frac{6}{\pi} \mathrm{Re}\left[\int \mathbf{J}(\mathbf{r})_i^* \cdot p(\mathbf{r}) d\mathbf{r} \right] \right\}, \tag{2}$$
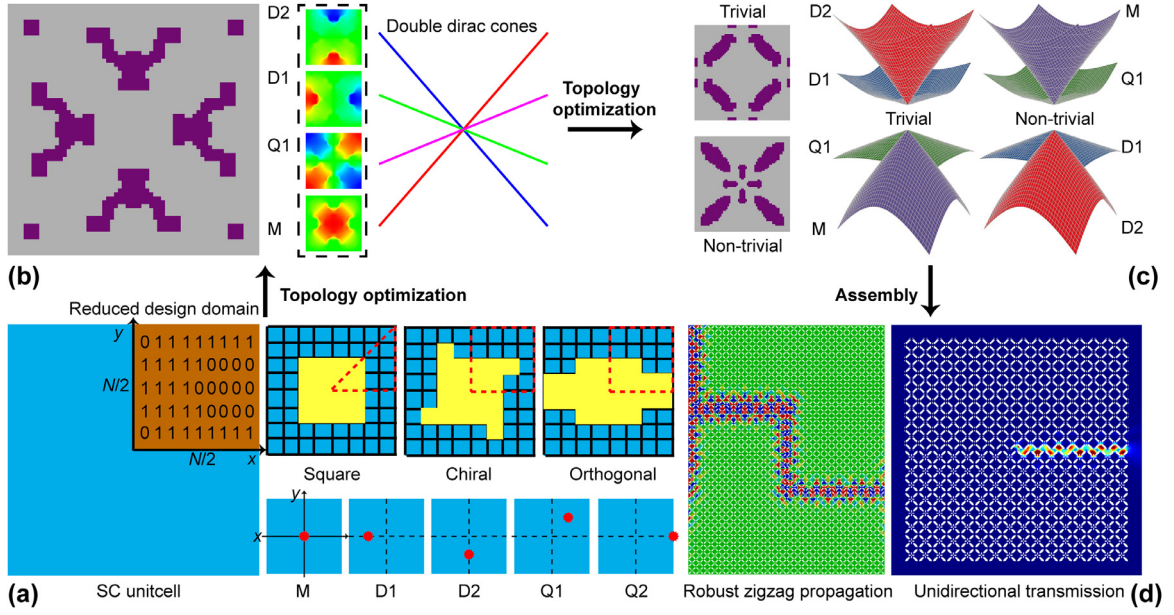
Fig. 1. Schematic of customized inverse design of acoustic Dirac cones and topological insulators using the bottom-up topology optimization. (a) A SC unitcell expressed by the $N \times N$ binary coding. The reduced design domains for three structural symmetries are denoted by the dash areas. For five expected eigenstates, the acoustic point sources marked by the red dots are applied in the specific locations. (b) A representative optimized SC unitcell with the double Dirac cones consisting of four degenerated modes M, D1, D2 and Q1. (c) Two representative optimized SC unitcells with the trivial and non-trivial bandgaps after the second step topology optimization. (d) Potential acoustic wave manipulations using the optimized pseudo-spin topological insulators.

$$Subject\ to : U_A(\Sigma) = 1, \tag{3}$$

$$\min_{\Sigma}(w_A,\ w_S) \geq a/32, \tag{4}$$

$$-\nabla \cdot \left[\rho(\mathbf{r})^{-1}\nabla p(\mathbf{r}) \right] - \omega^2 K(\mathbf{r})^{-1}p(\mathbf{r}) = i\mathbf{J}(\mathbf{r}), \tag{5}$$

where $N \times N$ represents the number of pixels used for a unitcell; ρ_i denotes the material density of a pixel in which 0 and 1 declare the air and solid materials, respectively; L_{min} is the object function representing the minimal radiated power; Σ denotes the discrete material distribution within a unitcell; N_S is the number of sources for the considered modes; $\mathbf{r}$ is the position vector; $\mathbf{J}(\mathbf{r}) = \delta(\mathbf{r} - \mathbf{r}_0)\hat{\mathbf{e}}_j e^{-i\omega t}$ is the radiated power in the direction of the unit directional vector $\hat{\mathbf{e}}_j$ at the position $\mathbf{r}_0$; p is the acoustic pressure; U_A is the number of the continuous air domains within a unitcell; w_A and w_S are the sets consisting of the widths of all air connections and solid connections within the unitcell, respectively; a is the lattice constant which is set at 0.032 m; ∇ declares the Laplace operator; and K is the bulk modulus. The geometrical constraint in Eq. (4) is imposed to accommodate the manufacturing requirements and to avoid resonances caused by very narrow air channels. To prevent the occurrence of infinite values of LDOS in optimization, parameters of acrylonitrile butadiene styrene (ABS) and air are selected as: $\rho_{ABS}=1230$ kg/m³ and $\rho_{AIR}=1.204$ kg/m³, $K_{ABS}=6.12 \times 10^9$ Pa and $K_{AIR}=(141921+141.921i)$ Pa. All calculations of LDOS in optimization are implemented by ABAQUS 6.14–1. The full wave simulations on cloaking and topological transmission are executed using ABAQUS and COMSOL Multiphysics 5.3, respectively.

In principle, the entire SC unitcell is regarded as the design domain in the topology optimization. If different assumed structural symmetries are considered, the design domain will be one-eighth or a quarter of the unitcell. As shown in Fig. 1(a), each element is represented by the material "0" (air) or "1" (solid). Then the corresponding binary matrix of $N \times N$ pixels becomes the design variables in the optimization. If a square symmetry is assumed, the design domain is reduced to one-eighth of the unitcell. For the chiral and orthogonal symmetries, the reduced design domain becomes a quarter of the unitcell. To apply Bloch theory, two opposite edges of the unitcell should have the same binary distribution. As a result, different symmetrical SC unitcells can be readily implemented in the proposed optimization procedure.

To clearly show the resulting monopolar, dipolar and quadrupolar modes, a sketch can be found in Fig. 1 to depict the location of the acoustic point source. For any given wave vector (k_x, k_y), the corresponding periodic boundary conditions are imposed on the four edges of the unitcell. To effectively excite the monopolar mode, the point source is put in the center of the unitcell. Upon reaching a monopolar resonance, the value of LDOS is maximized during the optimization. Similarly,

the point sources are put in other four locations (also shown in Fig. 1a) to excite other dipolar and quadrupolar modes. This excitation method can be easily extended to other lattice systems with an arbitrary Bloch wave vector.

After incorporating the given excitation source and structural symmetries, topology optimization can effectively generate the desired SC unitcell with the Dirac cone consisting of acoustic degenerate modes on demand, see the representative unti-cell possessing double Dirac cones in Fig. 1(b). If the further topology optimization is applied, two novel optimized unitcells with trivial and non-trivial bandgaps will be achieved at their prescribed degenerate frequencies, see Fig. 1(c). Finally, if two optimized unticells are assembly suitably, we can successively obtain the exceptional robust zigzag propagation and even unidirectional transmission as shown in Fig. 1(d).

In the GA optimization procedure, a population of chromosomes with binary matrices is first randomly generated. Then, the "abuttal entropy filter" [29] method is employed to improve the structural topology for preventing the extreme clutter geometries by filling up some isolated voids and removing some isolated elements, especially in the early stage of evolution. Secondly, the population of current generation will be evaluated for fitness function through Eqs. (2)-(5).

Specifically, considering the specific geometry constraints imposed in Eqs. (3) and (4), the optimization has to be performed interactively with structural analysis. Regarding the structural connectivity in Eq. (3), the optimization algorithm should carry out an image identification of the binary node-structure, i.e., determining the number of the connected air regions within the design domain and recording the corresponding number C_A. As for the minimal size constraint in Eq. (4), the algorithm should check the minimal sizes of all connected air and solid parts within the unitcell, i.e., recording the corresponding minimal feature values w_{MS} and w_{MA} for each unitcell. Comparing two arbitrary structures, i and j, the structure with a larger objective function L_{min} will be retained if both i and j are feasible solutions, i.e., satisfying all constraints of the optimization. If structure i is feasible but j is not, the algorithm will regard structure i as the better one. Otherwise, if both structures, i and j, are infeasible, the one with smaller C_A, w_{MS} and w_{MA} will be kept. After the above operations, the algorithm will force most structures involving GA to meet the geometry constraints in Eqs. (3) and (4) accordingly.

Thirdly, the tournament selection operation is applied for the current population to breed a new generation. Individual solutions are selected through a fitness-based process, where fitter solutions are more likely to be selected into the mating pool. Fourthly, the crossover and mutation operations are applied on the selected parent population for the offspring population. To accelerate the optimization process, the algorithm adopts the elitism strategy which ensures that the global best fitness is maintained between generations by copying the best chromosome from the previous generation into the next one. Finally, the optimization converges after a sufficient number of iteration and stops to give rise to a nearly optimal structure with the customized wave properties. In the subsequent simulations, the GA parameters are taken as: population size N_p=30, crossover probability P_c=0.9, mutate probability P_m=0.03, and the championship selection size N_c=21. Topology optimizations are executed in 32 × 32 pixels within 1500 generations and in 64 × 64 pixels within 1500 generations at the first and second stages, respectively. All optimizations are carried out on a Linux cluster with 16 cores of Intel Xeon E5–2660 at 2.20 GHz. And each run of our procedure takes about 11.66 h for an optimized unitcell.

Actually, topology optimization of LDOS by the gradient-based optimization algorithm (such as, SIMP method) is also entirely feasible for the present problem. The SIMP method exhibits two appealing advantages over other optimization methods: ease to be implemented for most structural and multi-physics optimization problems and high computational efficiency. Recently, the SIMP based on parallel technology provides an ideal platform for large-scale structural optimization problems. However, considering the complexity of the present problem including the multiple rigorous geometry constraints, various specific required eigenstates, different structural symmetries and arbitrary operating frequency, we opted for GA to effectively obtain various types of novel structures without any predetermined initial design, while keeping the computing cost at an acceptable level.

3. Optimized sonic crystals with predetermined dirac cones

Fig. 2 shows the optimized unitcells with Dirac cones exhibiting the predetermined double, triple and quadruple degeneracies with the predetermined resonance patterns and wave-vector points at the predetermined frequencies and structural symmetries, all being prescribed *a priori*. The optimization frequency errors at 12,000 Hz, 6000 Hz and 2000 Hz are as small as 2 Hz, 1 Hz and 0.1 Hz, respectively. It can be seen that all unitcells exhibit common topological features: 1) several discretely distributed solid blocks; 2) several open cavities located within the unitcell according to the structural symmetries; and 3) low symmetries of most solid blocks. In addition, the subwavelength (2000 Hz) S12 is significantly simpler than other Bragg-scattering (6000 Hz, 12,000 Hz) unitcells, i.e., only one chiral solid block combined with four chiral cavities. Due to the apparent resonance scattering feature, all Bragg-scattering eigenstates can be described as the multipolar Mie resonances. That is, because of the large impedance difference between the solids and the background air, optimized multi-cavities can effectively localize the acoustic waves in the interior domains, thus generating wave scattering governed by the local resonances, typical of Mie resonances [31,32]. Therefore, the multi-cavity structures with multipolar Mie resonances can not only warrant high-frequency arbitrary Dirac cones but also induce the negative and even zero effective properties. However, the low-frequency eigenstates of S12 are multipolar LC resonances (inductor-capacitor circuit) [31,32]. Specifically, four cavities and narrow air channels can be respectively equivalent to capacitances and inductances, thereby forming the typical multipolar LC resonances which can effectively realize the novel subwavelength Dirac cones and even broadband double negativities. Except the chiral cases, all orthogonal-symmetric unitcells with a double degeneracy have anisotropic dispersion surfaces. S13 with the quadruple degeneracy has high-symmetry surfaces (left). The other unit-cells
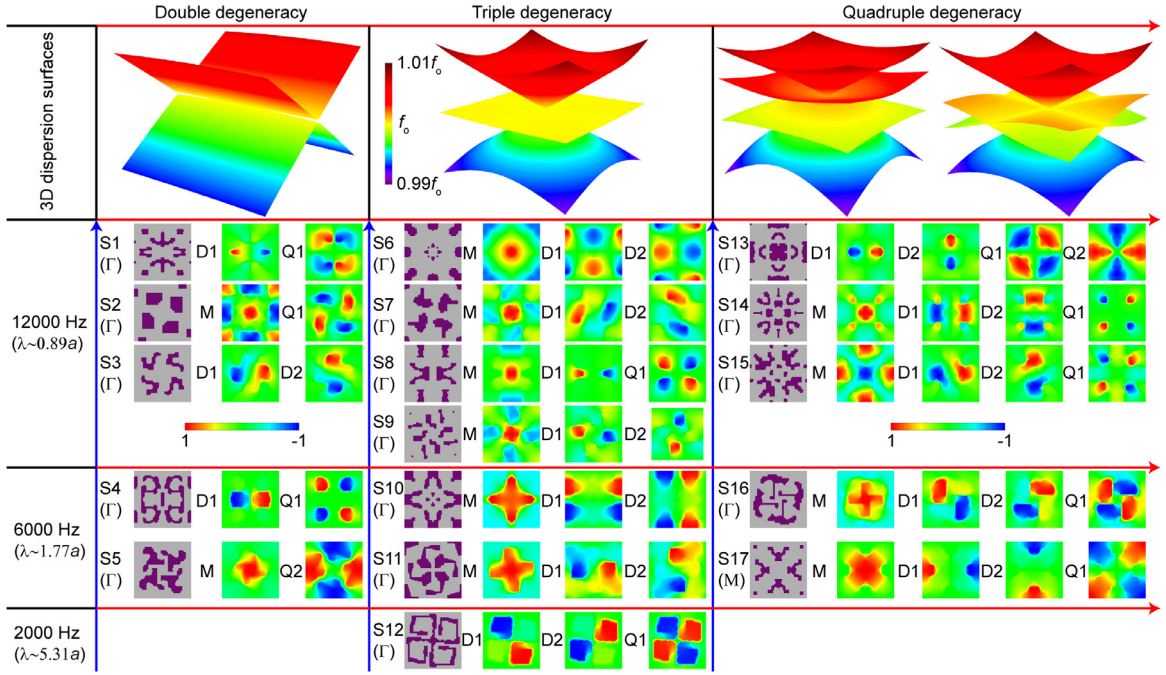
Fig. 2. Optimized SC unitcells with the customized Dirac cones supporting different types of the double (N_s=2), triple (N_s=3) and quadruple (N_s=4) degeneracies whose representative band structures are described by the 3D dispersion surfaces. Topologies and expected eigenstates are also shown for different wavelength scales. Purple and gray pixels respectively represent the solid and air mediums. Symbols Γ and M under the structure number denote the wave-vector points (k_x=0, k_y=0) and (k_x=π/a, k_y=π/a), respectively.

with the quadruple degeneracy have relatively low-symmetry surfaces (right). This indicates that the overall distribution of all eigenstates directly governs the symmetry of Dirac cones. Due to the inter-coupling or hybridization of local states, acoustic bands can be purposely adjusted through optimizing the topology by topology optimization. Finally, the energy and pressure field of the eigenstates can be obtained, thus realizing the Dirac cones on demand.

As shown in Fig. 2, it is noted that the small dots are inevitable during the topology optimization. Nevertheless, we made sure that all local small geometry features of the optimized unitcells satisfy the geometrical constraint in Eq. (4). In fact, the proposed filtering method aims at removing the isolated elements whose total sizes are smaller than a prescribed size, which in our case is set at $(a/32) \times (a/32)$=0.001 $m \times$ 0.001 m. As a result, the topology optimization can possibly construct an optimized unitcell with several isolated solid areas larger than 0.001 m. Of course, whether the generated topologies can have small isolated plastic regions depends on the optimization itself. Alternatively, we can increase the prescribed minimal size constraint to avoid the small blocks. However, both the resulting topology features and the operating frequency of a unitcell will be different.

Overall, most unitcells possessing Dirac cones with the customized double and triple degeneracies in Fig. 2 can enable zero-index peculiarity and allow the design of acoustic topological insulators with different mechanisms at different wave-vector points and different wavelength scales. More importantly, all five unitcells with the customized quadruple degeneracies can be regarded as the starting configurations for further constructing novel acoustic quantum spin-Hall acoustic topological insulators, highlighting the attractiveness of the customized inverse design for topological acoustics. A few typical wave propagation phenomena and the corresponding functionalities resulting from the above customized Dirac cones are illustrated hereafter. Of course, customizing the quintuple and even sextuple degeneracies may be a significant breakthrough in the future.

The combination of mode distribution and degeneracy type directly determine the wave properties of the optimized unitcells. More precisely, all unitcells with the double degeneracy can bring about the phase-reconstruction behavior at the Dirac point. For both triple and quadruple degeneracies, all unitcells can give rise to the zero effective index, thus leading to the cloaking and tunneling at the Dirac point. Of course, only the triple and quadruple degeneracies can be employed to further design the topological insulators. The distinct wave properties between them, however, is that the latter can support the topologically protected pseudo-spin edge states, while the former only can create the normal topologically protected edge states.

Particularly, irrespective of the structural symmetries that other optimized unitcells have, they can also be utilized to further design the acoustic topological insulators, as long as they can support the triple or quadruple degeneracy. All possible optimized topological insulators will naturally have different operating frequency ranges. In principle, there are two main differences between the topological insulators with triple and quadruple degeneracies. On one hand, the triple-degeneracy
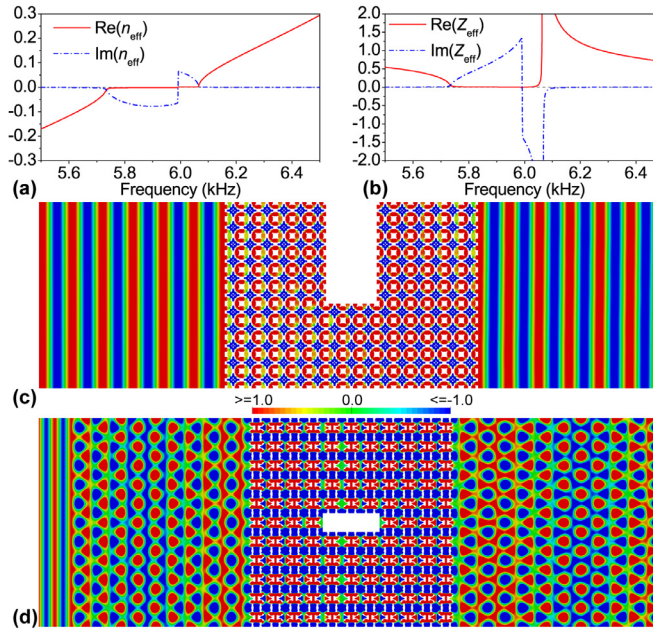
Fig. 3. (a)-(b) Relative effective refractive index n_{eff} and impedance Z_{eff} of S10 varying with the frequency. (c) Acoustic tunneling through a waveguide consisting of S10 at 6000 Hz. (d) Transmission showing the defect-immune property of a waveguide filled with S8 at 12,004 Hz.

enabled topological insulators can only be used for the full and robust zigzag transmission. But the quadruple-degeneracy enabled ones can induce both the robust transmission and the spin-hall unidirectional propagation. On the other hand, the quadruple-degeneracy enabled topological insulators usually require more isolated solid blocks than the triple-degeneracy enabled ones do.

4. Cloaking effects using customized dirac cones

Dirac cones can lead to zero effective index [15], tunneling [15], cloaking and collimation [33], etc. To further verify the customized Dirac cones, we examine the effective refractive index and impedance of S10, see Figs. 3(a) and 3(b). Clearly, $Re(n_{eff})$ gradually changes from the positive value to zero, while $Im(n_{eff})$ shifts near the Dirac point, implying the existence of resonance at the Dirac point. Similarly, $Im(Z_{eff})$ also shifts near the Dirac point while $Re(Z_{eff})$ decreases to a very small value. Consequently, S10 can induce the zero-effective index at the Dirac point. Fig. 3(c) shows that the incident plane wave can totally propagate through a U-shaped waveguide at the Dirac point, accompanied by a zero-phase change which confirms the zero index of S10.

Taking S8 as another example, we demonstrate the customized Dirac cones at a very high frequency. Fig. 3(d) shows that the outgoing wave-front has very similar shape with the incoming one near the triple Dirac degeneracy frequency. This is a typical feature of near-field diffraction Talbot effect [9], which is immune to the defect inside the waveguide. Although the effective medium theory cannot be applied, the high-frequency Dirac cones can realize the analogous cloaking effect.

5. Optimized topological insulators based on customized dirac cones

To show the potential of the customized Dirac cones in Fig. 2, we take S17 as an example and adopt the formulation in Eqs. (1)-(5) to perform another round of topology optimization in which S17 is employed as the initial configuration to construct two types of the SCs with different degeneracies at the M point. To demonstrate the accuracy of the optimization results, we intentionally select four randomly chosen frequencies as the target frequencies to achieve the double degeneracy, namely one structure supports two different dipole Mie resonances at 7840 Hz while the monopole and quadrupole Mie resonances at 4850 Hz. The other one supports monopole and quadrupole Mie resonances at 7920 Hz while two different dipole Mie resonances at 4960 Hz. Fig. 4(a) and 4(b) show that the two optimized SCs indeed contain trivial and non-trivial bands, respectively. Note that the topological phase transition is spontaneously induced near the double Dirac cones without any manual adjustment, demonstrating the universality and robustness of the proposed design strategy. Interestingly, S18 and S19 are essentially formed by the non-symmorphic symmetry operations and exhibit common topological feature, i.e., four big and several small solid blocks being symmetrically distributed in space. Since the double degeneracy states at the M point are pseudo-spin, the present topological phase transition mimics the quantum spin-Hall effect [9]. As shown in Fig. 4(c), the topological edge states emerge within [5776.1 Hz, 7855.6 Hz] with a relative bandwidth of 30.51%.
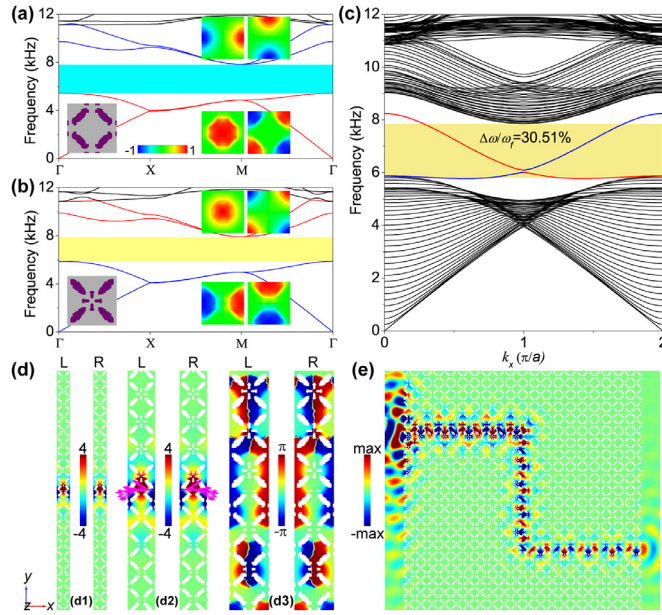
Fig. 4. (a)-(b) Band structures of the two optimized SCs (a: S18, b: S19) after the further TOPOLOGY OPTIMIZATION based on S17. Insets show the topologies and acoustic pressure fields of the double-degeneracy eigenstates at the M point. (c) Dispersion of the acoustic bulk (black) and edge (red and blue) states for supercells of S18 and S19. The periodic boundary conditions are imposed on the left and right edges of the supercell while the upper and lower edges are free. (d) Acoustic profiles of the pseudo-spin left and right edge states with the pressure (d1), Poynting vector (d2) and phase (d3) at the wave-vectors $(k_x=0.2\pi/a,\ k_y=0)$ (L) and $(k_x=1.8\pi/a,\ k_y=0)$ (R), respectively. The upper and lower half parts of the supercell are S19 and S18, respectively. (e) Simulated acoustic zigzag transmission using S18 and S19 at 7280 kHz.

The proposed methodology begins with a random configuration, which may not have been made very clear in the original paper. All optimized results presented in the paper are generated after 5 optimizations using the same algorithm parameters but with random initial population. As shown in Fig. 1, the inverse design strategy adopts a two-step bottom-up topology optimization strategy. In the first step, the optimized unitcell supporting the desired double, triple or quadruple degeneracy is produced at an arbitrary frequency. In the second step, the optimized unitcell with the Dirac cone on demand is further optimized to generate non-trivial and trivial unitcells at the prescribed frequencies for obtaining broadband topological insulators with the predetermined mechanism. Note that the first-step of the optimization starts with a random configuration, the outcome of which serves as the initial guess for the second-step. The most prominent feature of this two-step optimization approach is that we can obtain the topological insulators with the predetermined mechanism within a desired broadband range. Otherwise, if we combine the two-step approach into one-step, the final optimized unitcell can hardly achieve topological bandgap, not to mention the broadband property.

It is relevant to comment on the obtained broadband performance. In fact, most existing works on acoustic topological insulators offer narrow-band topological edge states which are limited by the empirical topologies of the unitcells. The first experimental airborne-sound topological insulators reported in the literature achieved the spin-hall acoustic topological insulators within [19.2 kHz, 20.5 kHz], corresponding to a relative bandwidth of 6.55% [6]. Another reported acoustic valley topological insulators can support the valley-selective protected edge states within [3.81 kHz, 4.33 kHz], namely a relative bandwidth of 12.78% [35]. A more effective topologically designed acoustic topological insulator based on spin-hall topological edge states reached a wider bandwidth of 12.5% [27]. Replacing triangle lattices by square lattices, a second-order acoustic topological insulator was shown to achieve both the protected edges and corner states within [9.5 kHz, 11.8 kHz] with a wider relative bandwidth of 21.6% [36]. Therefore, compared with previous studies, the presently achieved acoustic topological insulators with a relative bandwidth of 30.51% is record-breaking in topological acoustics. Theoretically, this broad topological bandgap can be further expanded if the difference between the upper and lower degeneracy frequencies becomes larger. As illustrated in Fig. 4(d), the edge states have nearly the same pressure distribution with the opposite phase and energy flow distribution. The phase singularity points around the phase winds $\pm 2\pi$ manifests the finite acoustic orbital angular momenta. Moreover, these vortices have the opposite phase winding directions for opposite propagation directions. Fig. 4(e) shows the full transmission through a zigzag waveguide with nearly full transmission with little backscattering, demonstrating the robustness of the topologically protected wave propagation.

6. Broad-band one-way transport using optimized topological insulators

To validate the above pseudo-spin topological states, Fig. 5 shows the acoustic wave propagation along the interface between S18 and S19 when a point-like chiral source is placed at the center of the model. In fact, each of the four acoustic
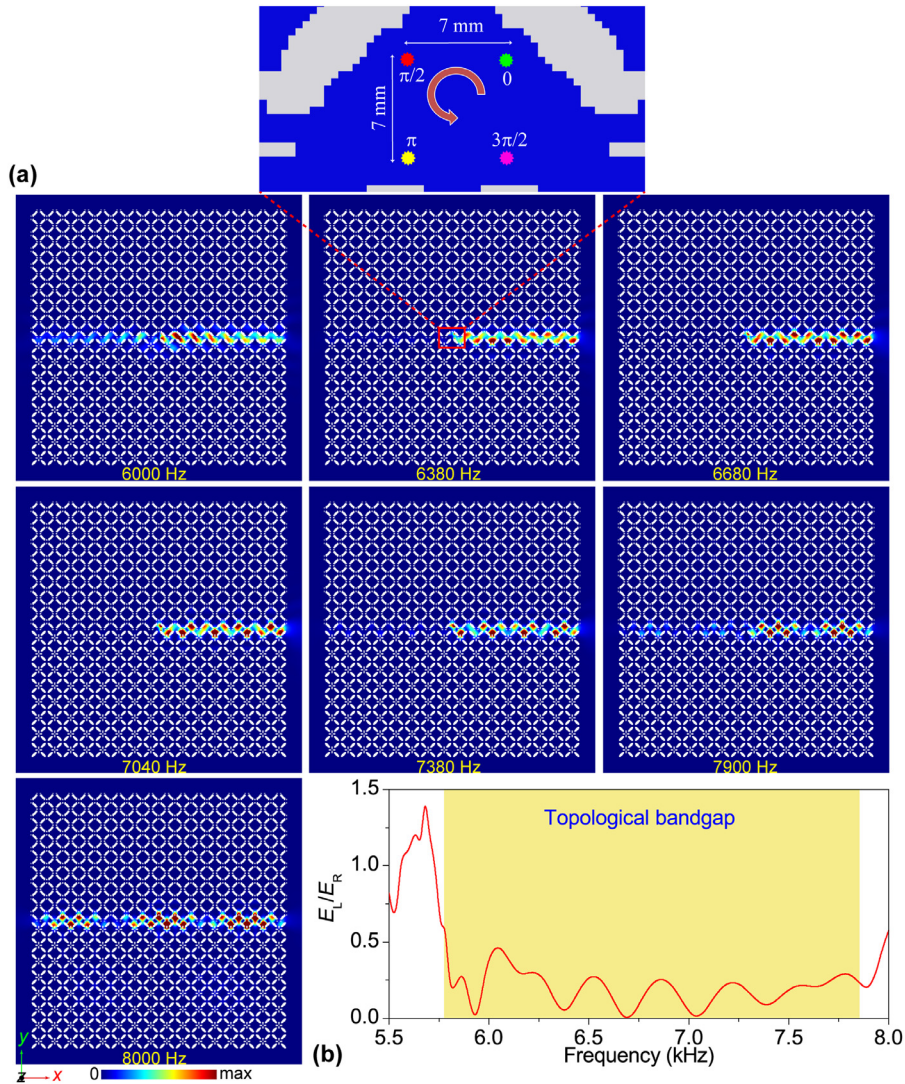
Fig. 5. (a)-(b) Simulated pseudo-spin dependent unidirectional transmission (a) and the transmission spectrum (b) using the optimized acoustic topological insulators in Fig. 2. E_L and E_R represent the left-port and right-port energy. The upper and lower half parts of the TIs are S18 and S19 in Fig. 4, respectively. The point-like chiral source carrying orbital angular momenta is excited by four acoustic point sources with an anticlockwise phase delay. The yellow shadow region represents the optimized topological bandgap range [5776.1 Hz, 7855.6 Hz].

sources is much smaller than the unitcell dimension (0.032 m). As shown in Fig. 5, the region surrounded by four point sources is 0.007 m × 0.007 m. Therefore, the total dimension of the chiral source cannot be neglected in simulation. Since the topology in Fig. 5 is opposite to that in Fig. 4(d), the edge states should mainly propagate along the positive *x*-direction if the source carries the anticlockwise orbital angular momenta. This is indeed the case, as illustrated in Fig. 5. Although a visible but small backscattering occurs in the opposite direction at the lower and higher frequencies, the nearly perfect unidirectional transport, originating from the spin-locked edge state propagation, can be achieved in a very broad topological range [5776.1 Hz, 7855.6 Hz], corresponding to a relative bandwidth of 30.51%. Once again, the achieved relative bandwidth largely exceeds those of the existing one-way transports ever realized by the electromagnetic and acoustic insulators, i.e., electromagnetic unidirectional range of [7.4 GHz, 7.56 GHz] with a relative bandwidth of 2.14% [37] and acoustic one-way range of [19.2 kHz, 20.5 kHz] with a relative bandwidth of 6.55% [6]. It can also be observed that, at the frequencies above the topological bandgap range, the propagation pattern starts to become nearly symmetric because only the bulk states exist, matching the band structures in Fig. 4(c).

Note that Fig. 5 shows visible backscattering. We would argue that this imperfection may be attributed to the specific energy distributions of the four degenerated modes, as illustrated in Figs. 4(a) and 4(b). However, the location and the size of the chiral source indeed slightly affect the efficiency of the unidirectional transmission. When the location of the source

moves downward, right-propagating transmission at lower frequencies is enhanced. Within the broad frequency range, perfect unidirectional transmission is realized near the center frequency of the defect band.

7. Conclusions

In conclusion, through a bottom-up topology optimization procedure, we have systematically achieved the customized acoustic Dirac cones and associated TIs based on the SCs in square lattices. Representative optimized SCs can realize the customized Dirac cones with various structural symmetries, resonance patterns and degeneracy mechanisms. With the optimized double Dirac cones, a further topology optimization gives rise to novel acoustic topological insulators with pseudo-spin edge states, entailing robust zigzag transmission and broadband unidirectional transport with the quantum spin-Hall effect. The achieved broadband performance, i.e. a relative bandwidth of 30.51% sets a new record by exceeding those ever reached previously. The present work paves the way towards an automatic construction and the customization of the degeneracy states and pseudo-spin states on demand and provides a general and robust framework for designing topological acoustics, with potential extension to optics [2] and elastics [15-18,34].

In future work, it is of interest to explore the design of 3D broadband high-order topological insulators using the present framework for robust and multifunctional 3D wave manipulations. Another avenue is to develop possible superior intelligent optimization models to realize acoustic topological insulators by only considering the performance of multiple degenerate modes. Aiming at perfect broadband topological insulators, it is also meaningful to minimize the existing backscattering issues by developing other novel topology optimization methodologies.

Declaration of Competing Interest

The authors declare that they have no known competing financial interests or personal relationships that could have appeared to influence the work reported in this paper.

CRediT authorship contribution statement

Hao-Wen Dong: Conceptualization, Methodology, Formal analysis, Visualization, Writing - original draft. **Sheng-Dong Zhao:** Software, Data curation, Validation. **Rui Zhu:** Formal analysis, Writing - review & editing. **Yue-Sheng Wang:** Supervision, Writing - review & editing, Project administration. **Li Cheng:** Supervision, Writing - review & editing, Project administration. **Chuanzeng Zhang:** Writing - review & editing, Project administration.

Acknowledgements

References

[1] L. Feng, Z.J. Wong, R.M. Ma, Y. Wang, X. Zhang, Single-mode laser by parity-time symmetry breaking, Science 346 (2014) 972–975.
[2] C. He, X.C. Sun, X.P. Liu, M.H. Lu, Y. Chen, L. Feng, Y.F. Chen, Photonic topological insulator with broken time-reversal symmetry, P. Natl. Acad. Sci. USA 113 (2016) 4924–4928.
[3] R. Fleury, D.L. Sounas, C.F. Sieck, M.R. Haberman, A. Alù, Sound isolation and giant linear nonreciprocity in a compact acoustic circulator, Science 343 (2014) 516–519.
[4] Z. Yang, F. Gao, X. Shi, X. Lin, Z. Gao, Y. Chong, B. Zhang, Topological acoustics, Phy. Rev. Lett. 114 (2015) 114301.
[5] R. Fleury, A.B. Khanikaev, A. Alù, Floquet topological insulators for sound, Nat. Commun 7 (2016) 1–11.
[6] C. He, X. Ni, H. Ge, X.C. Sun, Y.B. Chen, M.H. Lu, X.P. Lu, Y.F. Chen, Acoustic topological insulator and robust one-way sound transport, Nat. Phys. 12 (2016) 1124–1129.
[7] J. Lu, C. Qiu, M. Ke, Z. Liu, Valley vortex states in sonic crystals, Phy. Rev. Lett. 116 (2016) 093901.
[8] X. Ni, M. Weiner, A. Alù, A.B. Khanikaev, Nat. Mater. 18 (2019) 113–120.
[9] X. Zhang, H.X. Wang, Z.K. Lin, Y. Tian, B. Xie, M.H. Lu, Y.F. Chen, J.H. Jiang, Nat. Phys. 15 (2019) 582–588.
[10] Y. Ding, Y. Peng, Y. Zhu, X. Fan, J. Yang, B. Liang, X. Zhu, J. Cheng, Phy. Rev. Lett. 122 (2019) 014302.
[11] J. Lu, C. Qiu, L. Ye, X. Fan, M. Ke, F. Zhang, Z. Liu, Nat. Phys 13 (2017) 369–374.
[12] Z. Tian, C. Shen, J. Li, E. Reit, H. Bachman, J.E. Socolar, S.A. Cummer, T.J. Huang, Nat. Commun 11 (2020) 1–10.
[13] H. He, C. Qiu, L. Ye, X. Cai, M. Ke, F. Zhang, Z. Liu, Nature 560 (2018) 61–64.
[14] D. Torrent, J. Sánchez-Dehesa, Acoustic analogue of graphene: observation of Dirac cones in acoustic surface waves, Phy. Rev. Lett. 108 (2012) 174301.
[15] G. Ma, M. Xiao, C.T. Chan, Topological phases in acoustic and mechanical systems, Nat. Rev. Phys. 1 (2019) 281–294.
[16] S. Li, D. Zhao, H. Niu, X. Zhu, J. Zang, Observation of elastic topological states in soft materials, Nat. Commun. 9 (2018) 1–9.
[17] M. Serra-Garcia, V. Peri, R. Süsstrunk, O.R. Bilal, T. Larsen, L.G. Villanueva, S.D. Huber, Observation of a phononic quadrupole topological insulator, Nature 555 (2018) 342–345.
[18] S.Y. Yu, C. He, Z. Wang, F.K. Liu, X.C. Sun, Z. Li, H.Z. Lu, M.H. Lu, X.P. Liu, Y.F. Chen, Elastic pseudospin transport for integratable topological phononic circuits, Nat. Commun 9 (2018) 1–8.
[19] F. Liu, X. Huang, C.T. Chan, Dirac cones at k=0 in acoustic crystals and zero refractive index acoustic materials, Appl. Phys. Lett. 100 (2012) 071911.

[20] Y. Li, Y. Wu, J. Mei, Double Dirac cones in phononic crystals, Appl. Phys. Lett. 105 (2014) 014107.
[21] Z.G. Chen, X. Ni, Y. Wu, C. He, X.C. Sun, L.Y. Zheng, M.H. Lu, Y.F. Chen, Accidental degeneracy of double Dirac cones in a phononic crystal, Sci. Rep. 4 (2014) 1–7.
[22] Maznev, Dirac cone dispersion of acoustic waves in plates without phononic crystals, J. Acoust. Soc. Am. 135 (2014) 577–580.
[23] X.W. Yang, J.S. Lee, Y.Y. Kim, Effective mass density based topology optimization of locally resonant acoustic metamaterials for bandgap maximization, J. Sound Vib. 383 (2016) 89–107.
[24] O. Sigmund, M. Schevenels, B.S. Lazarov, G. Lombaert, Topology optimization of two-dimensional elastic wave barriers, J. Sound Vib. 376 (2016) 95–111.
[25] Y. Chen, F. Meng, G. Sun, G. Li, X. Huang, Topological design of phononic crystals for unidirectional acoustic transmission, J. Sound Vib. 410 (2017) 103–123.
[26] R.E. Christiansen, F. Wang, O. Sigmund, S. Stobbe, Designing photonic topological insulators with quantum-spin-Hall edge states using topology optimization, Nanophotonics 8 (2019) 1363–1369.
[27] R.E. Christiansen, F. Wang, O. Sigmund, Topological insulators by topology optimization, Phy. Rev. Lett. 122 (2019) 234502.
[28] Z. Lin, A. Pick, M. Lončar, A.W. Rodriguez, Enhanced spontaneous emission at third-order Dirac exceptional points in inverse-designed photonic crystals, Phy. Rev. Lett 117 (2016) 107402.
[29] H.W. Dong, S.D. Zhao, Y.S. Wang, C. Zhang, Topology optimization of anisotropic broadband double-negative elastic metamaterials, J. Mech. Phys. Solids 105 (2017) 54–80.
[30] H.W. Dong, S.D. Zhao, Y.S. Wang, C. Zhang, Broadband single-phase hyperbolic elastic metamaterials for super-resolution imaging, Sci. Rep 8 (2018) 2247.
[31] H.W. Dong, S.D. Zhao, P. Wei, L. Cheng, Y.S. Wang, C. Zhang, Systematic design and realization of double-negative acoustic metamaterials by topology optimization, Acta Mater 172 (2019) 102–120.
[32] H.W. Dong, S.D. Zhao, Y.S. Wang, L. Cheng, C. Zhang, Robust 2D/3D multi-polar acoustic metamaterials with broadband double negativity, J. Mech. Phys. Solids 137 (2020) 103889.
[33] M. Dubois, C. Shi, X. Zhu, Y. Wang, X. Zhang, Observation of acoustic Dirac-like cone and double zero refractive index, Nat. Commun 8 (2017) 1–6.
[34] S.S. Ganti, T.W. Liu, F. Semperlotti, Topological edge states in phononic plates with embedded acoustic black holes, J. Sound Vib. 466 (2020) 115060.
[35] J. Lu, C. Qiu, L. Ye, X. Fan, M. Ke, F. Zhang, Z. Liu, Observation of topological valley transport of sound in sonic crystals, Nat. Phys. 13 (2017) 369–374.
[36] X. Zhang, H.X. Wang, Z.K. Lin, Y. Tian, B. Xie, M.H. Lu, Y.F. Chen, J.H. Jiang, Second-order topology and multidimensional topological transitions in sonic crystals, Nat. Phys. 15 (2019) 582–588.
[37] Y. Yang, Y.F. Xu, T. Xu, H.X. Wang, J.H. Jiang, X. Hu, Z.H. Hang, Visualization of a unidirectional electromagnetic waveguide using topological photonic crystals made of dielectric materials, Phy. Rev. Lett. 120 (2018) 217401.
[38] S.S. Nanthakumar, X. Zhuang, H.S. Park, C. Nguyen, Y. Chen, T. Rabczuk, Inverse design of quantum spin hall-based phononic topological insulators, J. Mech. Phys. Solids 125 (2019) 550–571.
[39] Z. Du, H. Chen, G. Huang, Inverse design of quantum spin hall-based phononic topological insulators, J. Mech. Phys. Solids 135 (2020) 103784.